Journal of Advanced Marine Engineering and Technology, Vol. 49, No. 4, pp. 269~282, 2025
J. Advanced Marine Engineering and Technology (JAMET)
https://doi.org/10.5916/jamet.2025.49.4.269

ISSN 2234-7925 (Print)
ISSN 2765-4796 (Online)
Original Paper

Study on fluid flow and flow-induced noise simulation for a Circular Cylinder

Jae Hyeon Park[1] · Jun Ho Jeon[2] · Yeon Won Lee[†]

(Received July 30, 2025 ; Revised August 11, 2025 ; Accepted August 24, 2025)

Abstract: This study focuses on the aeroacoustic analysis of flow over a circular cylinder under subsonic conditions, with an emphasis on evaluating turbulence models and noise source treatment strategies. Unsteady flow simulations were conducted at a Reynolds number of $Re = 9 \times 10^4$ using RANS ($k-\epsilon$, $k-\omega$, and $k-\omega$ SST) and LES (Smagorinsky-Lilly, Dynamic Smagorinsky-Lilly, and WALE). Aerodynamic characteristics were analyzed based on separation point, drag coefficients, and Strouhal number. Flow-induced noise was computed using the Ffowcs Williams-Hawkings (FW-H) equation, with acoustic source extracted from both solid and permeable surfaces. This study examines the influence of turbulence model and noise source extraction methods for flow-induced noise simulation.

Keywords: Flow-induced noise, Turbulence model, FW-H equation, Permeable Surface, Circular cylinder flow

Nomenclature

ρ : Density [kg/m^3]
U_i : $Reynolds\ averaged\ velocity\ [m/s]$
p : $Pressure [Pa]$
u_i' : $Fluctuation\ velocity\ [m/s]$
μ : $Dynamic\ viscosity\ [Pa \cdot s]$
ν : $Kinematic\ viscosity\ [m^2/s]$
ν_t : $Turbulent\ viscosity\ [Pa \cdot s]$
k : $Turbulent\ kinetic\ energy\ [m^2/s^2]$
ϵ : $Dissipation\ of\ turbulent\ kinetic\ energy\ [m^2/s^3]$
ω : $Specificturbulencedissipationrate\ [s^{-1}]$
$\overline{u_i}$: $Gridscalevelocity\ [m/s]$
u_i' : $Subgrid\ scale\ velocity\ [m/s]$
τ_{ij} : $Viscous\ shear\ stress\ [kg/(m \cdot s^2)]$
μ_{SGS} : $SGS\ turbulent\ viscosity\ [Pa \cdot s]$
p' : $Pressure\ fluctuation\ [Pa]$
r: $Distance\ between\ the\ source\ and\ the\ observer\ [m]$
δ : $Dirac\ delta\ function$
v_i : $Velocity\ of\ moving\ body\ [m/s]$
M : $Mach\ number$
n : $Normal\ vector\ of\ the\ surface$
N : $Number\ of\ the\ grid\ points$
Re : $Reynolds\ number$
C_L' : $Root\ mean\ square\ error\ in\ lift\ coefficient$
$\overline{C_D}$: $Mean\ drag\ coefficient$
D : $Diameter\ of\ circular\ cylinder\ [m]$
f : $frequency\ [Hz]$
St : $Strouhal\ number$
θ_s : $Separation\ point\ angle\ [deg]$
SPL : $Sound\ pressure\ level\ [dB]$

1. Introduction

Noise is defined as pressure waves propagating through a fluid medium, generated by pressure fluctuations within the flow field. Among various types of noise, flow-induced noise is generated by complex fluid-dynamic mechanisms, including volumetric changes, interactions with solid surfaces, and turbulence. Because of these factors, it is regarded as a particularly challenging subject of analysis. Recently, the demand for accurate prediction and analysis of flow-induced noise has increased across diverse industries. Applications include noise reduction for rotating fluid

† Corresponding Author (ORCID: https://orcid.org/0000-0002-3749-8119): Professor, School of Mechanical Engineering, Pukyong National University, 45, Yongso-ro, Nam-gu, Busan, Korea, E-mail: ywlee@pknu.ac.kr, Tel: 051-629-6162
1 Ph. D. Candidate, Department of Mechanical and Robotics Engineering, Gwangju Institute of Science and Technology, E-mail: jay.park@gm.gist.ac.kr
2 Researcher, School of Mechanical Engineering, Pukyong National University, E-mail: skya333@naver.com.

machinery such as wind turbines**[1]**, ventilators**[2]**, and vertical take-off and landing (VTOL) vehicles**[3]**. In addition, flow noise issues are being addressed in large ships**[4]**, aircraft**[5]**, high-speed rail systems**[6]**, and wind effects around tall buildings**[7]**.

In flow-induced noise analysis, a method known as Computational Aeroacoustics (CAA) is commonly used, where acoustic sources are extracted using Computational Fluid Dynamics (CFD) and applied to acoustic analogies. The core of CAA is modeling complex flow-noise mechanisms and incorporate them into acoustic equations. Lighthill**[8][9]** was the first mathematically formalize the mechanisms of flow-induced noise, providing the theoretical foundation for subsequent studies. Before Lighthill, acoustic analogy formulations were based on linear equations, neglecting the nonlinearity of convective terms and limiting the analysis of turbulence noise. After Lighthill, Curle**[10]** and Doak**[11]** pointed out that only the nonlinear convective terms of the Lighthill equation remain significant in low-Mach number flow and proposed modifications to address this limitation. Subsequently, Ffowcs Williams and Hawkings**[12]** proposed the FW-H equation, which introduced the Heaviside function to model moving boundaries as well as reflection and refraction effects within flow fields. This formulation remains one of the most widely used tools in aeroacoustic analysis today.

Numerous studies have employed CFD in combination with the FW-H acoustic analogy to analyze flow noise generated around cylinders. Despite its simple geometry, the circular cylinder exhibits complex flow phenomena-adverse pressure gradients, flow separation, and vortex shedding-making it a widely recognized benchmark for validating turbulence model performance. Cox**[13]** investigated circular-cylinder flows in the subcritical to trans-critical Reynolds number using the RANS-based SST model. However, because a two-dimensional simulation was employed the predicted noise levels were approximately 25% lower than experimental results, while the first-harmonic frequency was overestimated by about 50%. Boudet**[14]** conducted LES-based simulations of circular-cylinder flows followed by aeroacoustic analysis, the predicted noise levels remained around 10% lower than measurements, and the frequency was similarly overpredicted, as in the RANS case. Escobar**[15]** and Orselli**[16]** performed three-dimensional simulations of circular and square cylinders using both RANS and LES, and the results varied substantially with the choice of turbulence model. These observations highlight the need to compare the accuracy of flow-noise predictions across turbulence models and to identify an appropriate computational approach.

In addition to these model-dependent discrepancies, Wang**[17]** noted, based on Proudman's acoustic-power analysis, that quadrupole noise sources at low Mach numbers are excluded in both the FW-H and Lighthill formulations, indicating the need for an alternative approach. In response, Bretner and Farassat**[18]** proposed reproducing quadrupole sources by placing a permeable surface around rotating blades. A permeable surface refers to a virtual boundary within the fluid domain, through which turbulence-induced monopole sources associated with fluid dilatation and dipole sources associated with pressure fluctuations can be represented to model turbulent noise generation.

In this study, flow-noise predictions for a circular cylinder were quantitatively compared across turbulence models based on LES and RANS, and their accuracy was evaluated against Revell's experimental data**[19]**. For LES, the Smagorinsky-Lilly, dynamic Smagorinsky-Lilly, and WALE(wall-adapting local eddy viscosity) models were applied. For RANS, the $\boldsymbol{k-\varepsilon}$, $\boldsymbol{k-\omega}$, $\boldsymbol{k-\omega}$ SST models were employed. In addition, a permeable surface was placed around the circular cylinder to examine the reproduction of quadrupole noise sources and to verify its accuracy. Furthermore, the effectiveness of quadrupole-source reconstruction via the permeable surface was compared with experimental results across the different turbulence models.

2. Numerical Analysis

2.1 RANS Model

In this study, the $k-\epsilon$, $k-\omega$ and $k-\omega$ SST models among the RANS models were employed. All of these are two-equation turbulence models, calculating turbulent viscosity μ_t by solving transport equations for turbulent kinetic energy k and either turbulent kinetic energy dissipation rate ϵ or specific turbulent dissipation rate ω.

First, in the $k-\epsilon$ model**[20]**, the transport equations for turbulent kinetic energy k and turbulent dissipation rate ϵ are expressed as **Equations (1)** and **(2)**, respectively. The turbulent viscosity μ_t is then calculated using **Equation (4)**.

$$\frac{Dk}{Dt} = P - \rho\epsilon + \frac{\partial}{\partial x_j}\left[\left(\mu + \frac{\mu_t}{\sigma_k}\right)\frac{\partial k}{\partial x_j}\right] + \rho L_k \tag{1}$$

$$\frac{D\epsilon}{Dt} = C_{\epsilon 1} f_1 \frac{\epsilon}{k} P - C_{\epsilon 2} f_1 \frac{\rho\epsilon^2}{k} + \frac{\partial}{\partial x_j}\left[\left(\mu + \frac{\mu_t}{\sigma_\epsilon}\right)\frac{\partial \epsilon}{\partial x_j}\right] + \rho L_\epsilon \tag{2}$$

Here, P represents the production term of turbulent kinetic energy k, defined as follows:

$$P = \mu_t \left(S_{ij} - \frac{1}{3}\frac{\partial u_k}{\partial x_k}\delta_{ij} \right) - \frac{2}{3}\rho k \delta_{ij} \tag{3}$$

The turbulent viscosity μ_t is subsequently calculated according to **Equation (4)**:

$$\mu_t = f_\mu C_\mu \frac{\rho k^2}{\epsilon} \tag{4}$$

Next, in the $k-\omega$ model**[21]**, the transport equations for turbulent kinetic energy k and specific turbulent dissipation rate ω are expressed as **Equations (6)** and **(7)**, respectively:

$$\frac{Dk}{Dt} = P - \beta^* \rho \omega k + \frac{\partial}{\partial x_j}\left[\left(\mu + \frac{\mu_t}{\sigma_k} \right) \frac{\partial k}{\partial x_j} \right] \tag{5}$$

$$\frac{D\omega}{Dt} = \frac{\gamma \omega}{k} P - \beta \rho \omega^2 + \frac{\partial}{\partial x_j}\left[\left(\mu + \sigma_\omega \frac{\rho k}{\omega} \right) \frac{\partial \omega}{\partial x_j} \right] + \frac{\rho \sigma_d}{\omega} \frac{\partial k}{\partial x_j} \frac{\partial \omega}{\partial x_j} \tag{6}$$

In the $k-\omega$ model, turbulent viscosity $\mu_t$is defined as shown in **Equation (7)**:

$$\mu_t = \frac{\rho k}{\widehat{\omega}} \tag{7}$$

The $k-\omega$ model employed in this study is based on the Wilcox $k-\omega$ model**[22]**, which utilizes a modified specific turbulent dissipation rate $\widehat{\omega}$ to partly address sensitivity issues in free-stream calculations. This modified dissipation rate is defined as follows:

$$\widehat{\omega} = \max\left[\omega, C_{lim} \sqrt{\frac{2\overline{S_{ij}}\,\overline{S_{ij}}}{\beta^*}} \right], \quad \overline{S}_{ij} = S_{ij} - \frac{1}{3}\frac{\partial u_k}{\partial x_k}\delta_{ij} \tag{8}$$

The $k-\varepsilon$ model is well suited for predicting free-stream flows but shows reduced accuracy in near-wall regions with strong adverse pressure gradients. Conversely, the $k-\omega$ model captures boundary-layer flows near wall more effectively, although it exhibits high sensitivity to inlet conditions in the free-stream regions**[23]**.

To overcome the limitations of these two models, Menter**[24]** proposed a hybrid model called the $k-\omega$ SST (Shear Stress Transport) model. This model is based on the transport equation of the specific turbulent dissipation rate ω in the $k-\omega$ model but introduces a blending function F_1 to switch the model depending on the flow region. Through this approach, the $k-\omega$ model is applied near the wall region, and the $k-\varepsilon$ model is applied in the free-stream region outside the boundary layer, allowing the advantages of both models to be utilized simultaneously**[25]**.

The transport equation of the specific turbulent dissipation rate ω for the $k-\omega$ SST model is expressed as **Equation (9)**, and the corresponding turbulent viscosity μ_t is defined by **Equation (10)**.

$$\frac{D\omega}{Dt} = \frac{\gamma}{\nu_t} P - \beta \rho \omega^2 + \frac{\partial}{\partial x_j}\left[(\mu + \sigma_\omega \mu_t) \frac{\partial \omega}{\partial x_j} \right] + 2(1 - F_1) \frac{\rho \sigma_{\omega 2}}{\omega} \frac{\partial k}{\partial x_j} \frac{\partial \omega}{\partial x_j} \tag{9}$$

$$\mu_t = \frac{\rho \alpha_1 k}{\max(a_1 \omega, \Omega F_2)} \tag{10}$$

The specific definitions and values of the turbulence model constants and limiters used in **Equations (1)** to **(10)** can be found in the related previous studies and references**[20]-[25]**.

2.2 LES Model

In LES, a key aspect is modeling the subgrid-scale (SGS) stress, τ_{ij}^{SGS}. As **Equation (11)**, this stress is a nonlinear residual term that arises from filtering the convective term.

$$\tau_{ij}^{SGS} = \rho\left(\overline{u_i u_j} - \overline{u}_i \overline{u}_j \right) \tag{11}$$

Similar to the treatment of turbulent viscosity μ_t in RANS, the SGS stress is represented using an SGS turbulent viscosity, μ_{SGS}, as follows**[26]**.

$$-\tau_{ij}^{SGS} = \mu_{SGS}\left(\frac{\partial \overline{u}_i}{\partial x_j} + \frac{\partial \overline{u}_j}{\partial x_i} \right) - \frac{2}{3}\left(\frac{\partial \overline{u}_k}{\partial x_k} \right)\delta_{ij} \tag{12}$$

LES turbulence models are commonly classified according to the definition of μ_{SGS}. In this study, the Smagorinsky-Lilly, dynamic Smagorinsky-Lilly, and WALE models were employed.

The Smagorinsky-Lilly model**[27]** introduces the length scale and velocity scale of eddies to model μ_{SGS}, which are defined as

follows.

$$l_m = C_s\zeta,\ \nu_m = l_m|\widetilde{S_{ij}}| \tag{13}$$

Here, C_s denotes the Smagorinsky constant. Lilly**[28][29]** suggested a value in the range $0.17 \le C_s \le 0.21$ based on Kolmogorov's turbulence energy spectrum through analysis of the inertial subrange of isotropic turbulence. However, such values may yield excessively high turbulent viscosity in near-wall regions, leading to abnormal dissipation of turbulent kinetic energy. Therefore, in this study, a value of $C_s = 0.1$, which has benn shown to provide empirically stable under various flow conditions, was adopted.

The Smagorinsky-Lilly model has a limitation in that its accuracy deteriorates near walls or in regions with rapidly changing flow characteristics when a constant C_s is used. To address this issue, the Dynamic Smagorinsky-Lilly model **[30]** was proposed. This model introduces an additional test filter with a larger scale than the grid filter. The characteristic length of the test filter ζ_{test} is typically set to be about 2 to 2.5 times larger than ζ that of the grid filter. The SGS stress with the test filter applied is defined as follows **[31]**.

$$T_{ij} = \rho\left(\widetilde{u_j u}_j - \tilde{u}_i\,\tilde{u}_j\right) \tag{14}$$

Meanwhile, the expression for the original SGS stress with the test filter applied as follows.

$$\tau_{ij}^{SGS} = \rho\left(\widetilde{u_i u_j} - \tilde{u}_i\,\tilde{u}_j\right) \tag{15}$$

Let the residual composed of the difference between the two stress terms be denoted as L_{ij}. In the Dynamic model, L_{ij} is modeled in the following form by relating it to tensor terms β_{ij} and α_{ij} which correspond to the structure of the Smagorinsky model.

$$\begin{aligned} &L_{ij} = C_s\left(\beta_{ij} - a_{ij}\right), \\ &\beta_{ij} = 2\zeta^2|\widetilde{S_{ij}}|\widetilde{S_{ij}},\ \alpha_{ij} = 2\widetilde{\zeta^2}|\widetilde{S_{ij}}|\widetilde{S_{ij}} \end{aligned} \tag{16}$$

At this point, the Smagorinsky constant C_s is dynamically computed using least squares minimization approach, as defined below[32].

$$C_s = \frac{L_{ij}\left(\beta_{ij} - \alpha_{ij}\right)}{\left(\beta_{ij} - \alpha_{ij}\right)^2} \tag{17}$$

The WALE model was proposed to address the issue of excessive turbulent viscosity predicted by the Smagorinsky model near wall regions. This model considers not only the strain rate tensor S_{ij} but also the rotation rate tensor Ω_{ij}, allowing it to capture the nonlinear characteristics of turbulent structures more accurately**[33]**. The SGS viscosity in LES model is generally expressed in the following form.

$$\mu_{SGS} = \rho(C_m\zeta)^2 \widetilde{OP(x,t)} \tag{18}$$

In the Smagorinsky-Lilly model, $\widetilde{OP(x,t)}$ is defined as $\widetilde{OP(x,t)} = \sqrt{2\,\widetilde{S_{ij}}\,\widetilde{S_{ij}}}$. However, in the WALE model, a new strain-rate-based tensor $S_{ij}^d$was introduced by Nicoud and Ducros**[34]**, and the formulation is constructed as shown in **Equation (19)**.

$$\begin{aligned} S_{ij}^d &= \widetilde{S_{ik}}\widetilde{S_{kj}} + \widetilde{\Omega}_{ik}\widetilde{\Omega}_{ik} \\ &-\frac{1}{3}\delta_{ij}\left(\widetilde{S_{mn}}\widetilde{S_{mn}} + \widetilde{\Omega_{mn}}\,\widetilde{\Omega_{mn}}\right) \end{aligned} \tag{19}$$

Accordingly, $\widetilde{OP(x,t)}$ is defined as follows.

$$\widetilde{OP(x,t)} = \frac{\left(S_{ij}^d S_{ij}^d\right)^{3/2}}{\left(\widetilde{S_{ij}}\widetilde{S_{ij}}\right)^{5/2} + \left(S_{ij}^d S_{ij}^d\right)^{5/4}} \tag{20}$$

Therefore, the SGS turbulent viscosity in the WALE model is determined as shown in equation (21).

$$\mu_{SGS} = \rho(C_m\zeta)^2\,\frac{\left(S_{ij}^d S_{ij}^d\right)^{3/2}}{\left(\widetilde{S_{ij}}\widetilde{S_{ij}}\right)^{5/2} + \left(S_{ij}^d S_{ij}^d\right)^{5/4}} \tag{21}$$

Nicloud proposed a model constant in the range of $0.55 \le C_m \le 0.6$, and in this study, a value of $C_m = 0.35$ was applied in consideration of numerical stability and convergence under various flow conditions.

2.3 FW-H Acoustic Analogy Equation

The FW-H equation is an acoustic analogy used to predict noise sources by accounting for the motion of solid boundaries and pressure fluctuations within unsteady flow fields. It is expressed as shown in **Equation (22)[12]**.

$$\left(\frac{\partial^2}{\partial t^2} - c^2\frac{\partial^2}{\partial x_i^2}\right)\rho' = \tag{22}$$

$$\frac{\partial^2 T_{ij}^L}{\partial x_i \partial x_j} - \frac{\partial}{\partial x_i}\left(P_{ij}\delta(f)|\nabla f|\right) + \frac{\partial}{\partial t}(\rho_0 v_i \delta(f)|\nabla f|)$$

Here, ρ′represents the acoustic perturbation variable induced by unsteady variations in the flow field, and f is a function used to describe the interior and exterior of a solid object–taking values $f(x,t) < 0$ inside the object, $f(x,t) > 0$ outside, and $f(x,t) = 0$on the surface. This definition allows for the continuous representation of the geometric location of the boundary surface, enabling efficient incorporation of surface integral information in the FW-H equation.

Additionally, $P_{ij} = \mathrm{p}\delta_{\mathrm{ij}} - \tau_{\mathrm{ij}}$, where τ_{ij} denotes the viscous stress, and v_i represents the velocity component of the moving solid boundary.

In **Equation (22)**, the right-hand side of the FW-H equation is classified according to physical characteristics as follows. The first term represents a volume source term, corresponding to a quadrupole noise source generated by turbulence and compressibility effects. The second term is a dipole noise source caused by fluctuations in the stress acting on the solid surface, commonly referred to as loading noise. The third term corresponds to a monopole noise source, generated by the motion of the solid boundary or volumetric changes in the fluid, and is classified as thickness noise.

Here, T_{ij}^L is the Lighthill stress tensor, which mathematically represents the volume noise source generated by turbulence and compressibility effects within the flow field. It is defined as shown in **Equation (23) [9]**.

$$T_{ij}^L = \rho' u_i u_j + p'\delta_{ij} - \rho' c^2 \delta_{ij} + \tau_{ij} \quad (23)$$

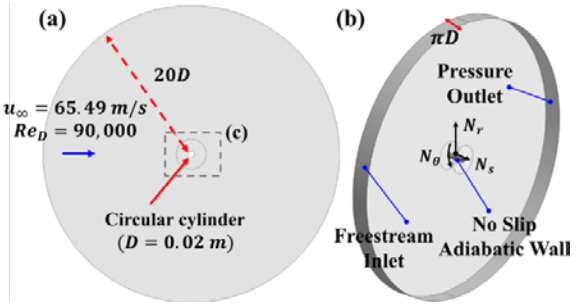

Figure 1. Computational domain and grid configuration for analysis: (a) A Planer view of the circular domain with inlet velocity and Re number; (b) boundary conditions and grid inside in cylindrical Coordinate (N_r, N_θ, N_s)

To capture the major noise sources generated by turbulence in the flow field, a virtual permeable surface was defined to enclose the object. This approach integrates the noise sources based on flow variables on a specific control surface within the flow field**[34]**. In particular, when the surface is positioned in regions of high turbulence intensity, it can effectively capture quadrupole noise sources through monopole noise induced by fluid volumetric changes and dipole noise caused by lift force fluctuations. Therefore, in this study, the FW-H equation with a permeable surface was applied to evaluate the characteristics of flow-induced noise under subsonic conditions.

2.4 Flow Analysis Model for Circular Cylinder

For the fluid flow and acoustic analysis of the circular cylinder, the computational domain was configured in a circular shape, as shown in **Figure 1(a)**. The diameter of the target circular cylinder is $D = 0.02m$, the inlet velocity is $u_\infty = 65.49\mathrm{m/s}$ and the Reynolds number is $Re_D = 9.0 \times 10^4$. The radial boundary of the flow domain extends up to a distance of 20D from the center of the cylinder, and the spanwise domain length is set to πD.

Regarding boundary conditions, a freestream inlet condition was applied on the upstream hemispherical boundary, and a pressure outlet condition was applied on the downstream side. On the surface of the cylinder, no-slip and adiabatic boundary conditions were imposed. For the turbulent models, freestream turbulent intensity set to I=0.5% and relative freestream $k_\infty, \varepsilon_\infty$, and $\omega_\infty$are set as follows:

$$k_\infty = \frac{3}{2}(U_\infty I)^2$$

$$\varepsilon_\infty = C_\mu^{3/4}\frac{k_\infty^{3/2}}{0.07D}$$

$$\omega_\infty = \frac{\varepsilon_\infty}{C_\mu k_\infty}$$

The mesh system was constructed based on a cylindrical coordinate system and is defined by the number of divisions in the radial (N_R), azimuthal (N_θ), and spanwise (N_S)directions (see **Figure 1(b)**). For the RANS analysis, three grid resolutions—Coarse, Medium, and Fine—were designed for grid convergence evaluation. **Table 1** compares the enlarged grid structure near the cylinder used in both LES and RANS analyses.

Figure 2 shows the results of the grid dependency test conducted for the RANS cases. It was observed that, for all RANS

Table 1: Grid information for Coarse, Medium, Fine case of RANS

Case	N_r, N_θ, N_s	Total
Coarse	$125 \times 304 \times 20$	7.5×10^5
Medium	$250 \times 304 \times 20$	15.0×10^5
Fine	$350 \times 304 \times 20$	21.0×10^5

Table 2: Simulation settings for circular cylinder flow

Software	Ansys FLUENT R 20.2[37]
Algorithm	PISO Algorithm
Flow Analysis	
Simulation Type	Transient
Time Step	$5.36 \times 10^{-5} sec$
Total Time	0.3216 sec (6.000 times)
Acoustic Analysis	
Simulation Type	Transient
Time Step	$5.36 \times 10^{-6} sec$
Total time	0.0804 sec (15,000 times)

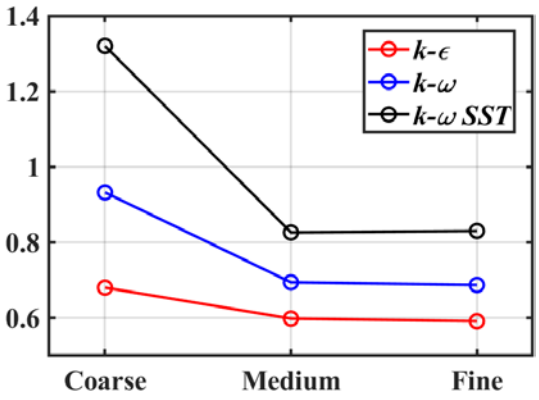

Figure 2: Grid convergence test for RANS turbulence model

turbulence models, the drag coefficient of the circular cylinder remains nearly constant beyond the medium grid resolution. Based on this, the medium grid was selected for further analysis in the RANS simulations.

In the case of LES, more than 80% of the total turbulent kinetic energy must be resolved directly without relying on the SGS (Subgrid-Scale) model. To satisfy this criterion, the turbulent kinetic energy (k) and its dissipation rate (ϵ) must meet the following conditions.

$$\Delta \sim \frac{1}{5}\frac{k^{3/2}}{\epsilon} \tag{24}$$

In this context, the number of grid cells for LES analysis was determined based on the turbulent kinetic energy k and its dissipation rate ε obtained from the RANS analysis. The final grid configuration was set to $N_r \times N_\theta \times N_s = 350 \times 304 \times 40$, resulting in a total of 42.0×10^5 cells. Additional details related to the flow simulation settings are summarized in **Table 2**. In the Table 2, The acoustic analysis requires a smaller time step than the flow analysis to accurately capture the propagation of pressure perturbations to the receiver.

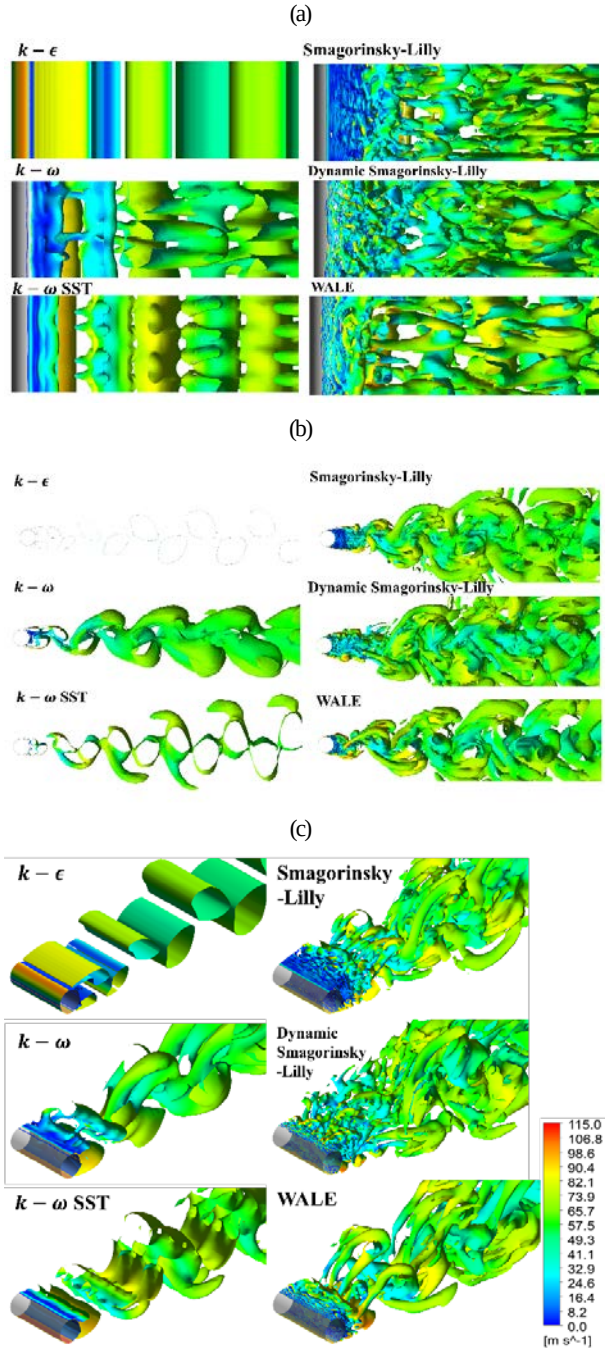

Figure 3: Vortex structures in the wake of a circular cylinder visualized using the Q-criterion (Q=0.01) for various models (a) Top view, (b) Front view and (c) Isometric view

3. Results and Discussion

3.1 Fluid flow Analysis Results

Figure 3 presents the visualization of vortex structures formed in the wake of a circular cylinder for various turbulence models using the Q-criterion (Q = 0.01). The RANS-based $k-\epsilon$ model exhibits spanwise-averaged flow, showing two-dimensional flow characteristics despite being a three-dimensional computation.

This is evident in **Figure 3(b)**, where almost two dimensional vortex structures are formed in the front view, and is further supported by the uniform spanwise velocity component observed in the top view in **Figure 3(a)**. In contrast, both the $k-\omega$ and $k-\omega$ SST models show more regular vortex structures in the spanwise direction and demonstrate the progression of vortices in the streamwise direction.

The LES-based Smagorinsky-Lilly, Dynamic Smagorinsky-Lilly, and WALE models capture three-dimensional turbulent structures with high fidelity. As shown in **Figure 3(c)**, the vortex shedding phenomenon and complex vortex interactions in the wake of the cylinder are clearly represented. Among these, the WALE model successfully simulates flow structures even near the wall, and it reveals distinct spanwise flow non-uniformity and turbulence structures. This is because the WALE turbulence model accounts for the nonlinear vortex structures of turbulence through the deformation tensor S_{ij}^{d}. Overall, it is clear that LES models captures wake vortex structures with higher accuracy and more realistic physical representation compared to RANS models.

Table 3 compares the aerodynamic characteristics of the circular cylinder for six turbulence models with experimental results reported by West**[38]**, Achenbach**[39]**, Cantwell**[40]**, and Norberg**[41]**. Among the comparison parameters, the frequency (f) refers to the fluctuation frequency of the lift coefficient caused by vortex shedding around the cylinder. The Strouhal number is the nondimensional form of this frequency and is defined as follows:

$$St = \frac{fD}{u_{\infty}} \tag{24}$$

According to the results in Table 3, the RANS model failed to adequately reproduce the aerodynamic characteristics of the circular cylinder. In particular, the RMSE of the lift coefficient oscillations and the drag coefficient values were significantly underpredicted compared with the experimental data. Moreover,

Table 3: Comparison between experimental data and CFD simulation results for circular cylinder flow (SL*: Smagorinsky-Lilly model)

	C_L' RMSE Lift Coefficient	$\overline{C}_D$ Mean Drag Coefficient	C_D' RMSE Drag Coefficient
Exp.[38-41]	0.45 – 0.60	1.0 – 1.4	0.18 – 0.21
SL*	0.044	0.89	0.024
Dynamic SL*	0.42	1.05	0.162
WALE	0.45	1.07	0.172
$k-\epsilon$	0.069	0.60	3.88×10^{-4}
$k-\omega$	0.22	0.69	0.0154
$k-\omega$ SST	0.50	0.83	0.040
	f [Hz]	St $\frac{f\times D}{u_{\infty}}$	θ_s Separation Point
Exp.[38-41]	589 – 625.4	0.180 – 0.191	80°
SL*	703	0.215	82.8°
Dynamic SL*	597	0.182	80°
WALE	632	0.193	80°
$k-\epsilon$	775	0.237	109°
$k-\omega$	735	0.225	101°
$k-\omega$ SST	818	0.25	103°

the frequency and Strouhal number (St) associated with the lift coefficient oscillations were overestimated, and the separation point appeared to be delayed. In contrast, the LES results showed that the Smagorinsky-Lilly model predicted the separation point relatively well, but it still failed to accurately capture the aerodynamic characteristics such as the lift and drag coefficients.

Among the LES models, the Dynamic Smagorinsky-Lilly and WALE models exhibited aerodynamic characteristics most consistent with the experimental results. Their predictions exists within the range of the reference experimental data, indicating that these turbulence models are capable of reliably capturing aerodynamic behavior. In contrast, the RANS models predicted an excessively delayed separation point, leading to vortex-shedding frequencies and drag-coefficient fluctuations that deviated substantially from the physical phenomena. Furthermore, the LES Smagorinsky-Lilly model suggested that the use of a fixed C_s coefficient is insufficient to represent complex flow behavior.

Figure 4 shows the comparison of the pressure coefficient (C_p)

along the surface of the circular cylinder, measured clockwise from the stagnation point 0° to 180°. In the favorable pressure gradient region, all turbulence models exhibit similar pressure distributions regardless of model type. However, in the adverse pressure gradient region, distinct differences are observed in both the separation point and pressure distribution depending on the turbulence model. In particular, the RANS models predict flow separation at a location delayed by approximately 20°or more compared to the LES models, resulting in a noticeable deviation from the actual physical behavior.

The reason for the delayed separation point in RANS models can be identified through the streamline distributions shown in **Figure 5**. In the LES-based Dynamic Smagorinsky-Lilly and WALE models, small-scale vortices that separate from the cylinder surface and are ejected outward are clearly observed. A large vortex structure, denoted as A, forms in the wake of the cylinder and simultaneously interacts through shear mechanisms with a counter-rotating vortex B located beneath it, as well as with surrounding small-scale vortices (A'). These multi-scale shear interactions effectively facilitate the transfer of turbulent energy, enabling the separation point to be modeled in a manner consistent with experimental observations.

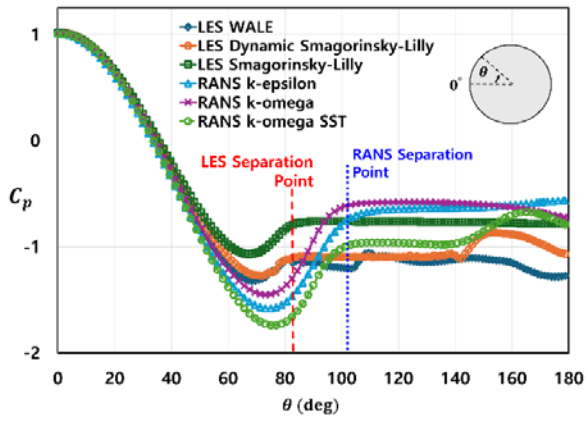

Figure 4: Pressure coefficient along azimuthal angle at cylinder surface

In contrast, the RANS model based on the $k-\omega$ SST formulation forms only large-scale vortices A and B in the wake of the cylinder, while small-scale vortices are not observed. As a result, the turbulence structures in the wake region are simplified, and shear interactions are weakened. This ultimately leads to a downstream delay in the flow separation point. In practice, flow separation occurs around 80° in the LES models, whereas in the $k-\omega$ SST model, separation occurs at approximately 100° to 110°.

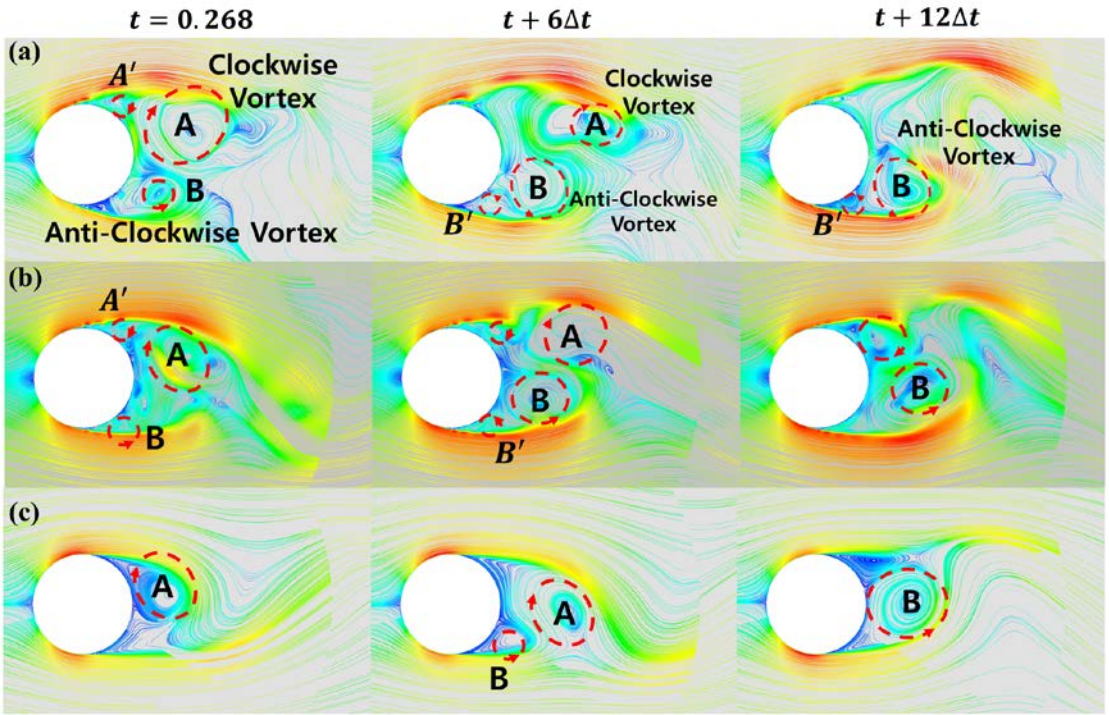

Figure 5: Streamline behind the circuluar cylinder with time increasement $\Delta t = 5.36 \times 10^{-4}$ for dynamic Smagorinsky-Lilly (a), WALE (b), and $k-\omega$ SST (c)

This delayed separation leads to a reduction in pressure drag, which explains why the drag coefficient predicted by the RANS-based analysis is lower than both the experimental data and the LES results.

In conclusion, based on quantitative comparisons with experimental results and the physical interpretation of the flow structures, the turbulence models that most realistically reproduce the flow characteristics and aerodynamic behavior in the wake of a circular cylinder are the LES-based Dynamic Smagorinsky-Lilly and WALE models.

3.2 Acoustic Analysis Results

The unsteady flow results of the circular cylinder obtained from the CFD analysis in Section 3.1 are used as input data for flow-induced noise analysis. In particular, the time-dependent pressure fluctuations serve as the acoustic source term in the FW-H equation. The solution computed via the FW-H equation is expressed in the form of $p'(x,t)$, where x denotes the observer

location and t represents the time at which the noise reaches that location. The acoustic pressure obtained in the time domain through the FW-H equation is transformed into the frequency domain sound pressure level (SPL) using the Fast Fourier Transform (FFT), and is defined as follows:

$$SPL\,[dB] = 20\log_{10}\left(\frac{p'}{p_{ref}}\right), \quad p_{ref} = 2\times10^{-5}\ \text{Pa} \tag{26}$$

The flow considered in this study corresponds to a subsonic condition with a Mach number of approximately $M \approx 0.2$, in which the contribution of quadrupole noise is relatively small. Therefore, the volume source term representing quadrupole sources plays a limited role. To account for this, a virtual permeable surface was defined at a radial distance of $2.5D = 0.05m$, which corresponds to the region where vortex shedding is most intense. Based on the monopole and dipole source terms extracted from the flow field within this region, an acoustic analysis was conducted to reconstruct the quadrupole noise.

In the flow-induced noise analysis, the observer location was set at a radial distance of $r = 2.438m$ and at an angular position $\theta = 90°$from the center of the circular cylinder. This configuration matches the measurement conditions used in Revell's experiment**[19]** and was adopted in this study to validate the accuracy and reliability of the proposed aeroacoustic analysis method.

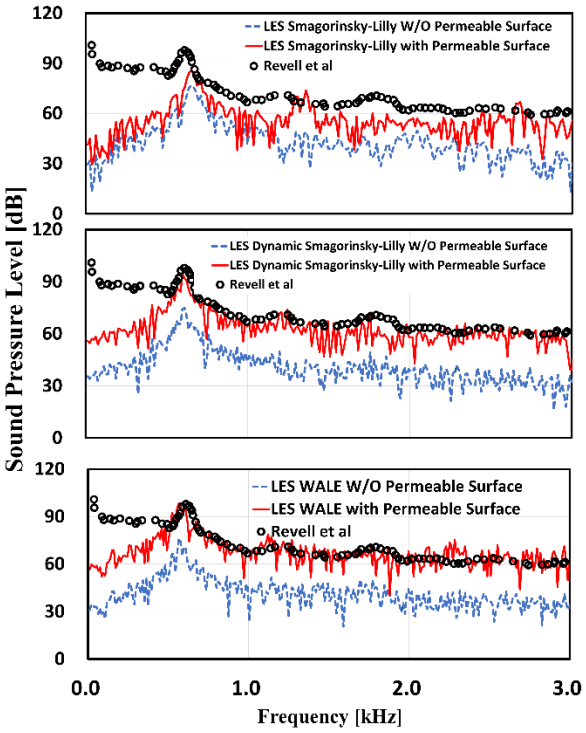

Figure 6: Comparison of sound pressure level spectra with or without permeable surface using LES turbulence model: Smagorinsky-Lilly(top), Dynamic(middle), and WALE(bottom) **[19]**

Figure 6 presents the results of flow-induced noise analysis using LES-based turbulence models, comparing the SPL spectra with and without the application of a permeable surface. When the permeable surface was not applied, all three LES models showed SPL values in the range of 74.8 to 77 dB at the first harmonic frequency, which is significantly lower than the 97.9 dB reported in Revell's experiment. This discrepancy is attributed to the relatively low flow Mach number ($M \approx 0.2$), which limits the contribution of turbulence-induced quadrupole sources in the FW-H equation.

In contrast, when the permeable surface was applied, all LES models showed a significant increase in SPL values. Notably, the Dynamic Smagorinsky-Lilly model yielded 94.3 dB, and the WALE model reached 97.8 dB, both closely matching the experimental value. Furthermore, the WALE model not only reproduced the SPL at the first harmonic accurately but also exhibited a spectral distribution in the high-frequency range that closely resembled the experimental results, demonstrating the highest predictive accuracy among the LES turbulence models.

Figure 7 shows the results of flow-induced noise analysis performed using RANS-based turbulence models. Similar to LES models, the RANS models also exhibited an increase in SPL

values when the permeable surface was applied. However, the magnitude of this increase was relatively smaller ranging from 9.9 to 11.3 dB compared to the 8.4 to 21.5 dB range observed in LES. This suggests that the RANS models are unable to resolve the fine-scale vortices in the wake of the cylinder, limiting the effective transmission of turbulence-induced noise source through the permeable surface. As a result, none of the RANS models achieved SPL values comparable to the experimental results, providing quantitative evidence of their lower noise prediction accuracy relative to the LES models.

The improvement observed with the permeable surface arises because it directly transmits the unsteady flow structures within its control volume into the acoustic field. In the case of LES, fine-scale vortices and shear-layer interactions are resolved with higher fidelity, producing localized monopole and dipole sources that the permeable surface can effectively capture and radiate as acoustic waves. This mechanism explains enhanced SPL predictions and closer agreement with experimental data in LES. By contrast, RANS models suppress such small-scale fluctuations through Reynolds averaging, preventing the permeable surface from effectively converting them into acoustic sources, which in turn results in weaker SPL amplification.

Table 4 summarizes the harmonic frequencies and corresponding SPL values calculated for each turbulence model, with and without the application of the permeable surface. This allows for a clear comparison of the flow-induced noise prediction performance across different turbulence models.

Table 4: Predicted Flow induced noise at 1st harmonic frequency and SPL for each turbulence model ($r = 2.438m$, $\theta = 90°$, SL* : Smagorinsky-Lilly)

	Exp.[19]	LES SL*		LES Dynamic SL*		LES WALE	
		w/o	with	w/o	with	w/o	with
f [Hz]	609	660	64.8	610	598	566	576
SPL [dB]	97.9	77	85.4	74.8	94.3	76.3	97.8
	Exp.[19]	RANS $k-\epsilon$		RANS $k-\omega$		RANS $k-\omega$ SST	
		w/o	with	w/o	with	w/o	with
f [Hz]	609	884	884	809	809	810	810
SPL [dB]	97.9	70.5	80.9	72.9	84.2	77.8	87.7

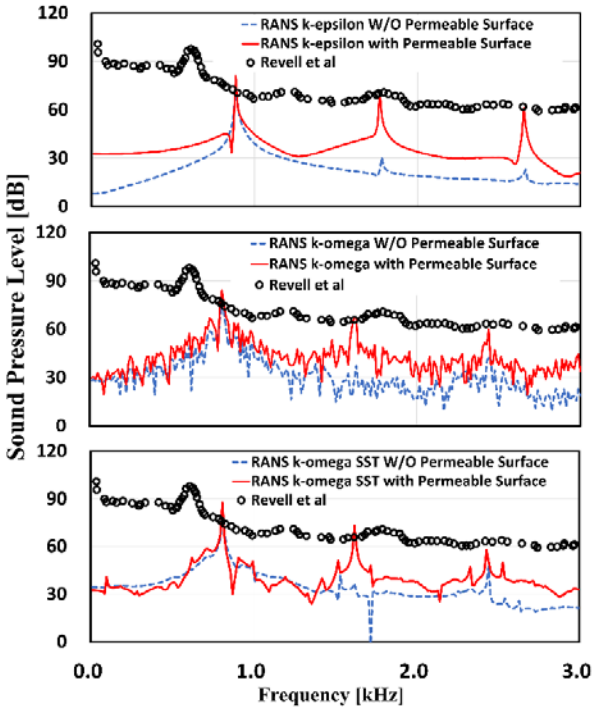

Figure 7: Comparison of sound pressure level spectra with or without permeable surface using RANS turbulence model: $k-\epsilon$(top), $k-\omega$(middle), and $k-\omega$ SST (bottom)**[19]**

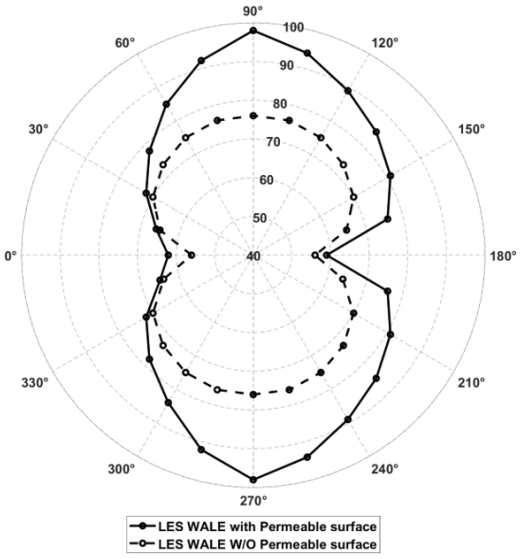

Figure 8: Sound pressure level calculated using the LES WALE model for each direction at $r = 2.438m$ and comparison with or without permeable surface

Figure 8 illustrates the acoustic radiation pattern computed at the observer location ($r = 2.438m$) using the LES-based WALE model. When the permeable surface was not applied, the dominant noise source was the dipole-type radiation caused by

pressure fluctuations on the cylinder surface, resulting in a symmetric sound field with clearly defined radiation directions.

In contrast, with the permeable surface applied, additional noise sources induced by turbulence in the flow field were captured, leading to an overall increase in SPL in all directions. Notably, the largest increase in sound pressure was observed in the $\theta = 90^\circ$ and $\theta = 270^\circ$ directions.

When the permeable surface is not applied, turbulence-induced noise sources are not accounted for, and the dominant noise source becomes the dipole noise generated by pressure

fluctuations on the solid surface. The radiation characteristics of such dipole sources are proportional to $cos\theta$, resulting in minimum sound pressure levels at $\theta = 0^\circ$ and $\theta = 180^\circ$, where the observer is aligned with the front and rear of the cylinder.

On the other hand, when the permeable surface is applied and turbulence-induced noise sources are included, the quadrupole term in the FW-H equation is additionally considered. Quadrupole noise sources typically exhibit a $cos^2\theta$ directional pattern, leading to maximum sound pressure levels at $\theta = 90^\circ$ and $\theta = 270^\circ$. Thus, it can be confirmed that in these directions, turbulence-induced noise is predominantly radiated.

Figure 9 presents the SPL frequency spectra at observer positions located in the $\theta = 0^\circ$(**Figure 9(A)**) and $\theta = 90^\circ$(**Figure 9(B)**) directions, at distances of 0.5 m, 1.0 m, and 2.438 m. In both directions, the frequency spectra of SPL exhibit similar distribution patterns, indicating that the dominant acoustic frequency components remain consistent regardless of distance. On the other hand, as the observer location becomes closer to the noise source, the overall SPL level increases, confirming that SPL is dependent on both distance and direction. However, the dominant frequency components themselves are determined by direction (angle) and are not affected by distance. This trend is also confirmed by the quantitative results shown in **Table 5**.

Table 5: 1st harmonic frequency and amplitude of SPL with permeable surface using LES WALE model

Direction	A(0°)			B(90°).		
Distance	0.5m	1m	2.438m	0.5m	1m	2.438m
f [kHz]	1.12	1.12	1.12	0.576	0.576	0.576
SPL [dB]	75	70	62	112	106	98

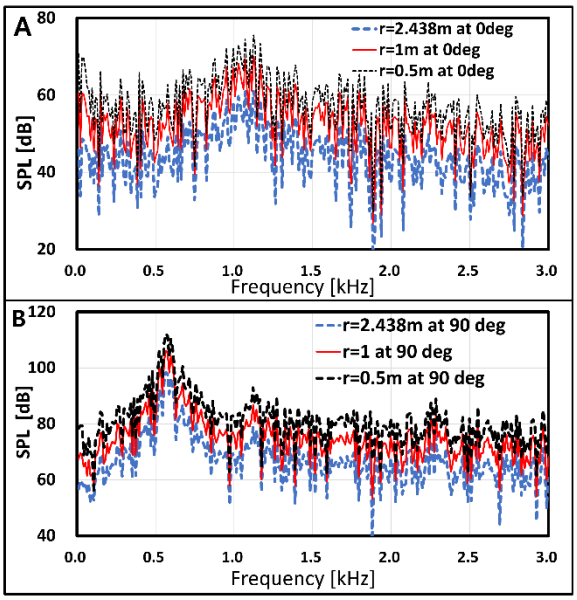

Figure 9: SPL spectra with permeable surface using LES WALE model. A(0°) and B(90°).

4. Conclusion

In this study, aerodynamic and flow-induced noise analyses of a circular cylinder were performed using RANS- and LES-based turbulence models, with particular attention to the role of permeable surface effects. The results were quantitatively compared with Revell's experimental data to assess both turbulence model performance and the reliability of the FW-H acoustic analogy with permeable surfaces.

1) From the aerodynamic analysis, LES-based models, particularly the Dynamic Smagorinsky-Lilly and WALE models, showed predictions of drag coefficient, Strouhal number, and separation point within the range of experimental data. In contrast, all RNAS models underpredicted drag coefficients, overpredicted Strouhal numbers, and delayed separation compared with the experiments. These results indicate that LES models provide more reliable aerodynamic predictions than RANS models.
2) In the acoustic analysis, all turbulence models underpredicted the SPL at the first harmonic frequency without the permeable surface with deviations exceeding 10 dB form the experimental value of 97.9 dB. When the permeable surface was applied, the LES models exhibited SPL increases of about 20-22 dB, reducing the error to within 2 dB of the experiment. Among them, the WLAE model showed the closest agreement at 97.8 dB. In contrast, the RANS models showed smaller SPL increases of 9.9 -11.3

dB, and their predictions remained at least 10 dB lower than the experimental value.

3) Overall, the results confirm that LES-based models, particularly the WALE and Dynamic Smagorinsky-Lilly, achieve the highest accuracy for both aerodynamic and acoustic predictions of a circular cylinder under subsonic conditions. Furthermore, the analysis highlights the importance of incorporating turbulence-induced sources via a permeable surface for reliable flow-induced noise prediction.

This study confirmed that LES-based models, particularly WALE and Dynamic Smagorinsky-Lilly, provided the most reliable aerodynamic and acoustic predictions among the turbulence models tested. At the same time, the use of permeable surface was shown to be crucial for accurate FW-H noise prediction, However, the analysis was limited to a single Reynolds number and circular cylinder geometry under subsonic conditions, which constrains the generality of the conclusions. Future work should therefore extend this framework to broader Reynolds numbers, different geometries, and more complex flows to enhance its applicability to practical aeroacoustic design.

Acknowledgement

This work was supported by the Research-Year Faculty Support Program of Pukyong National University in 2023. And this paper is a revised and expanded version of the first author's master thesis.

Author Contributions

Conceptualization, J. H. Park and Y.W. Lee; Methodology, J. H. Park; Software, J. H. Park; Validation, J. H. Park and J. H. Jeon; Formal Analysis, J. H. Park and J. H. Jeon; Investigation, J. H. Park; Data Curation, J. H. Park; Writing-Original Draft Preparation, J. H. Park; Writing-Review & Editing, J. H. Jeon and Y. W. Lee; Visualization, J. H. Park; Supervision, Y. W. Lee.

References

[1] E. Pedersen and K. P. Waye, "Prediction and annoyance due to wind turbine noise-a dose-response relationship," The Journal of the Acoustical Society of America, vol. 116, no. 6, pp. 3460-3470, 2004.

[2] D. Huff, "Fan noise prediction-status and needs," In 36th AIAA Aerospace Sciences Meeting and Exhibit, AIAA-1998-0177, 2012.

[3] S. A. Rizzi, *et al.*, Urban Air Mobility Noise: Current Practice, Gaps, and Recommendations, NASA Technical Paper 20205007433, 2020.

[4] D. Wittekind and M. Schuster, "Propeller cavitation noise and background noise in the sea," Ocean Engineering, vol. 120, pp. 116-121, 2016.

[5] W. Dobrzynski, H. Buchholz, W. Dobrzynsky, and H. Buchholz, "Full-scale noise testing on Airbus landing gears in the German Dutch wind tunnel," In 3rd AIAA/CEAS Aeroacoustics Conference, AIAA-1997-1597, 1997.

[6] C. Mellet, F. Letourneaux, F. Poisson, C. Talotte, "High speed train noise emission: latest investigation of the aerodynamic/rolling noise contribution," Journal of Sound and Vibration, vol. 293, no. 3, pp. 535-546, 2006.

[7] Y. D. Kim, J. Yohanes, and S. N. Kim, "A study on numerical simulation on flow-fields & wind-induced noise around buildings," Journal of the Wind Engineering Institute of Korea, vol. 12, no. 3, pp. 159-164, 2008 (in Korean).

[8] M. J. Lighthill, "On sound generated aerodynamically I. General theory," Proceedings of the Royal Society of London Series A. Mathematical and Physical Sciences, vol. 211, no. 1107, pp. 564-587, 1952.

[9] M. J. Lighthill, "On sound generated aerodynamically II. Turbulence as a source of sound," Proceedings of the Royal Society of London Series A. Mathematical and Physical Sciences, vol. 222, no. 1148, pp. 1-32, 1954.

[10] N. Curle, "The influence of solid boundaries upon aerodynamic sound," Proceedings of the Royal Society of London Series A. Mathematical and Physical Sciences, vol. 231, no. 1187, pp. 505-514, 1955.

[11] P. E. Doak, "Acoustic radiation from a turbulent fluid containing foreign bodies," Proceedings of the Royal Society of London Series A. Mathematical and Physical Sciences, vol. 254, no. 1276, pp. 129-146, 1960.

[12] J. F. Williams and D. L. Hawkings, "Sound generation by turbulence and surfaces in arbitrary motion," Philosophical Transactions for the Royal Society of London Series A. Mathematical and Physical Sciences, vol. 264, no. 1151, pp. 321-342, 1969.

[13] J. S. Cox, C. L. Rumsey, K. S. Brentner, and B. A. Younis, "Computation of vortex shedding and radiated sound for a circular cylinder," In ASME International Mechanical Engineering Congress and Exposition, IMECE 1997-0088, 1997.

[14] J. Boudet, D. Casalino, M. Jacob, and P. Ferrand, “Prediction of sound radiated by a rod using large eddy simulation,” In 9th AIAA/CEAS Aeroacoustics Conference and Exhibit, AIAA 2003-3217,2003.

[15] M. Escobar, I. Ali, C. Hahn, M. Kaltenbacher, and S. Becker,
“Numerical and experimental investigation on flow induced noise from a square cylinder,” In 10th AIAA/CEAS Aeroacoustics Conference, AIAA 2004-3004, 2004.

[16] R. Orselli, J. Meneghini, and F. Saltara, “Two and three-dimensional simulation of sound generated by flow around a circular cylinder,” In 15th AIAA/CEAS Aeroacoustics Conference, AIAA 2009-3270, 2009.

[17] M. Wang, S. K. Lele, and P. Moin, “Computation of quadrupole noise using acoustic analogy,” AIAA Journal, vol. 34, no. 11, pp. 247-254, 1996.

[18] K. S. Bretner and F. Farassat, “Analytical comparison of the acoustic analogy and Kirchhoff formulation for moving surfaces,” AIAA Journal, vol. 36, no. 8, pp. 1379-1386, 1998.

[19] J. D. Revell, R. A. Prydz, and A. P. Hays, “Experimental study of aerodynamic noise vs. drag relationships for circular cylinder,” AIAA Journal, vol. 16, no. 9, pp. 889-897, 1978.

[20] K. Y. Chien, “Predictions of channel and boundary-layer flows with a low-Reynolds number turbulence models,” AIAA Journal, vol. 20, no. 1, pp. 33-38, 1982.

[21] D. C. Wilcox, “Comparison of two-equation turbulence models for boundary layers with pressure gradient,” AIAA Journal, vol. 31, no. 8, pp. 1414-1421, 1993.

[22] D. C. Wilcox, “Formulation of the k-omega turbulence model revisited,” AIAA Journal, vol. 46, no. 11, pp. 2823-2838, 2008.

[23] J. C. Kok, “Resolving the dependence on freestream values for the k-turbulence model,” AIAA Journal, vol. 38, no. 7, pp. 1292-1295, 2000.

[24] F. R. Menter, “Performance of popular turbulence model for attached and separated adverse pressure gradient flows,” AIAA Journal, vol. 30, no. 8, pp. 2066-2072, 1992.

[25] F. R. Menter, “Two-equation eddy-viscosity turbulence models for engineering applications,” AIAA Journal, vol. 32, no. 8, pp. 1598-1605, 1994.

[26] A. Leonard, “Energy cascade in large-eddy simulations of turbulent fluid flows,” Advances in Geophysics, vol. 18, pp. 237-248, 1975.

[27] J. Smagorinsky, “General circulation experiments with the primitive equations: I. The basic experiment,” Monthly Weather Review, vol. 91, no. 3, pp. 99-164, 1963.

[28] D. K. Lilly, “On the application of the eddy viscosity concept in the inertial sub-range of turbulence," National Center for Atmospheric Research Report, 1966.

[29] D. K. Lilly, "The representation of small-scale turbulence in numerical simulation experiments," Proceedings of the IBM Scientific Symposium on Environmental Science, pp. 195-210, 1967.

[30] M. Germano, U. Piomelli, P. Moin, and W. H. Cabot, "A dynamic subgrid-scale eddy viscosity model," Physics of Fluids A: Fluid Dynamics, vol. 3, no. 7, pp. 1760-1765, 1991.

[31] C. Meneveau and J. Katz, “Scale-invariance and turbulence models for large-eddy simulation,” Annual Review of Fluid Mechanics, vol. 32, no. 1, pp. 1-32, 2000.

[32] D. K. Lilly, “A proposed modification of the Germano subgrid-scale closure method,” Physics of Fluids A: Fluid Dynamics, vol. 4, no. 3, pp. 633-635, 1992.

[33] S. T. Bose and G. I. Park, “Wall-modeled large-eddy simulation for complex turbulent flows,” Annual Review of Fluid Mechanics, vol. 50, pp. 535-561, 2018.

[34] F. Nicoud and F. Ducros, “Subgrid-scale stress modelling based on the square of the velocity gradient tensor,” Flow, Turbulence, and Combustion, vol. 62, no. 3, pp. 183-200, 1999.

[35] F. Farassat, Derivation of Formulations 1 and 1A of Farassat, NASA Technical Memorandum 2007-214853, 2007.

[36] K. S. Brentner and F. Farassat, “Analytical comparison of the acoustic analogy and Kirchhoff formulation for moving surfaces,” AIAA Journal, vo. 36, no. 8, pp. 1379-1386, 1998.

[37] ANSYS, 2020, ANSYS FLUENT User's Manual Version 20.2, ANSYS Inc.

[38] G. S. West and C. J. Apelt, “Measurements of fluctuating pressures and forces on a circular cylinder in the Reynolds number range,” Journal of Fluids and Structures, vol. 7, no. 3, pp. 227-244, 1993.

[39] E. Achenbach, “Distribution of local pressure and skin friction around a circular cylinder in cross-flow up to $Re = 5 \times 10^6$,” Journal of Fluid Mechanics, vol. 34, no. 4, pp. 625-639, 2006.

[40] B. Cantwell and D. Coles, “An experimental study of entrainment and transport in the turbulent near wake of a circular cylinder,” Journal of Fluid Mechanics, vol. 136, pp. 321-374, 1983.

[41] C. Norberg, “Fluctuating lift on a circular cylinder: review and new measurements,” Journal of Fluids and Structures, vol. 17, no. 1, pp. 57-96, 2003.